Estimation of the Hourly Aerosol Optical Depth From GOCI Geostationary Satellite Data: Deep Neural Network, Machine Learning, and Physical Models

Jong-Min Yeom, Seungtaek Jeong, Jong-Sung Ha, Kwon-Ho Lee, Chang-Suk Lee, and Seonyoung Park

***Abstract*—In this study, a new deep learning method was developed to estimate the spatiotemporal properties of the hourly aerosol optical depth (AOD) because existing physical models are limited in their abilities to separate the reflectance between aerosols and the underlying surface over land, accurately and effectively. By incorporating geostationary ocean color imagery (GOCI), multispectral bands were applied to train data-driven models to estimate the high-spatiotemporal-resolution AOD over Northeast Asia. Physical model and traditional machine learning (ML) models (the random forest (RF) and support vector regression (SVR) models) were compared with the deep neural network (DNN) model to evaluate its accuracy, implementing hold-out validation and k-fold cross-validation approaches. In the statistical results of the hold-out validation, the DNN model showed the higher accuracy (root mean square error (RMSE) = 0.112, mean bias error (MBE) = 0.007, and correlation coefficient (R) = 0.863) relative to the traditional SVR (RMSE = 0.123, MBE = −0.010, and R = 0.833) and RF (RMSE = 0.125, MBE = 0.004, and R = 0.825) models. The DNN model also exhibited the best performance for most statistical metrics among the traditional SVR, RF, and selected physical models (except for the correlation coefficients and index of agreement) in the spatial and temporal cross-validation analyses. Although the DNN model was trained using the match-up dataset between the top of atmosphere (TOA) reflectance from GOCI multispectral bands and AErosol RObotic NETwork measurements, it showed high spatial and temporal generalization performance owing to its deeper and more complicated network structure. Hourly GOCI AOD data obtained using a deep learning approach with high accuracy are expected to be useful for the quantification of aerosol contents and monitoring of diurnal variations in the AOD.**

***Index Terms*—Aerosol optical depth (AOD), deep neural network (DNN), geostationary ocean color imagery (GOCI) satellite, Northeast Asia, random forest (RF), support vector regression (SVR).**

I. INTRODUCTION

THE aerosol optical depth (AOD) has been one of the major atmospheric parameters used in climate change and air pollution research. Atmospheric aerosols influence the climate system directly by scattering or absorbing incident solar radiation on Earth [1]–[3] and indirectly by altering cloud microphysical properties and their lifetimes [4]–[7]. Uncertainty in aerosol radiative forcing is a major challenge in climate studies [8]. In addition to climate change, atmospheric aerosols have significant effects on human health; a rapid increase in the particulate matter (PM) mass concentration in a short period is associated with hospital admissions due to respiratory problems [9], [10]. Aerosols have inhomogeneous spatial and temporal distributions as a consequence of their short lifetimes. Therefore, accurately determining the loading and properties of aerosols is important for understanding their direct and indirect effects on the climate system and public health.

Aerosols can be monitored by estimating their optical properties from the AErosol RObotic NETwork (AERONET) using ground-based sun photometers [11] or using airborne and satellite instrumentation [12], [13]. The main advantage of AERONET is to secure the accuracy of aerosol optical properties (AOPs) and loadings using upward spectral channels of ground-based sun photometers with high temporal resolution. However, AERONET stations are too sparse to monitor the spatial characteristics of AOPs because the spatiotemporal variations and optical properties of atmospheric aerosols are unpredictable and complicated, and it is difficult to cover large spatial domains only using ground-based measurements. Therefore, satellites are considered as alternatives to monitor the spatiotemporal variations in AOPs over large areas. Several methods of estimating AOD over land and ocean have been developed using polar orbits, such as the Moderate Resolution Imaging Spectroradiometer [14]–[18], Sea-viewing Wide Field-of view Sensor [19]–[21], Medium Resolution Imaging Spectrometer (MERIS) [22], and geostationary satellites, such as the Geostationary Operational Environmental Satellite [23], [24], Multifunctional Transport

Manuscript received January 5, 2021; revised May 11, 2021 and July 16, 2021; accepted August 7, 2021. Date of publication September 9, 2021; date of current version January 21, 2022. This work was supported by Seoul National University of Science and Technology and Korea Aerospace Research Institute. *(Corresponding author: Seonyoung Park.)*

Jong-Min Yeom, Seungtaek Jeong, and Jong-Sung Ha are with the Satellite Application Division, Korea Aerospace Research Institute, Daejeon 34133, Republic of Korea.

Kwon-Ho Lee is with the Department of Atmospheric and Environmental Sciences, Gangneung-Wonju National University, Gangneung 25457, Republic of Korea.

Chang-Suk Lee is with the Climate and Air Quality Research Department, Environmental Satellite Center, National Institute of Environmental Research, Incheon 22689, Republic of Korea.

Seonyoung Park is with the Department of Applied Artificial Intelligence, Seoul National University of Science and Technology, Seoul 01811, Republic of Korea (e-mail: sypark@seoultech.ac.kr).

Digital Object Identifier 10.1109/TGRS.2021.3107542

SATellites [25], Spinning Enhanced Visible and Infra-Red Imager [26]–[28], and Geostationary Ocean Color Imagery (GOCI) [29]–[31]. Although these satellites are effective in estimating spatiotemporal variations in the AOD with the state-of-the-art sensors, satellite-based AOD products still have uncertainties owing to cloud masking, aerosol model assumptions, and surface reflectance. A key problem with using satellite images to retrieve aerosol properties is the difficulty of effectively separating and explicitly describing the contributions of reflectance from the underlying surface and backscattering from semi-transparent aerosol particles to the signal observed by the satellite-based instrument at the top of the atmosphere (TOA) [32]–[34]. Estimating the AOPs from satellite data and calculating them separately are difficult because optical satellites in orbit inevitably observe mixed spectral signals for both the atmosphere and land surface [35]. Therefore, we must develop new approaches to improve the accuracy of the AOD using satellite data to evaluate air pollution exposure for climate change and epidemiological studies, as well as for public health concerns.

Data-driven machine learning (ML) models show outstanding accuracy in the retrieval and prediction of the AOD and PM [36]–[39]. They are also useful for predictions in nonlinear system modeling and control [37], [40], [41]. ML models do not require information on the physical processes related to the radiative dynamics of aerosols, but they require complex mathematical equations for the atmosphere [42], [43].

Several ML approaches, such as artificial neural networks (ANNs), support vector regression (SVR), and the random forest (RF) method, have effectively predicted the AOD or other geophysical products [44]–[50]. Although these models have performed well, they have shown limitations in some studies. ANN models produce less accurate atmospheric forecasts than the existing ML models [51] under severe weather conditions [52]. Although SVR exhibits low sensitivity to high dimensionality and is unlikely to suffer from data dimensionality [53], it has difficulty with complicated nonlinearities in the atmosphere when using big data. The RF model tends to be overfitted closer to the mean value when there are an insufficient number of extreme samples because it was developed based on the lowest prediction error [54]. Therefore, a feasibility study of the improved data-driven approaches is required because rendering the ML models as more complex networks would be effective to reflect the nonlinear and complicated aerosol scattering or absorption processes in the atmosphere [36], [55]. Recently, based on the development of high-performance computing, deep learning approaches have been considering major breakthroughs in solving the challenges in geophysical research [35], [51], [56]–[60].

In this study, we retrieved the hourly AOD data using GOCI incorporated with a deep neural network (DNN) over Northeast Asia. For the first time, the DNN method was applied to estimate the spatiotemporal variations in the AOD over Northeast Asia using geostationary satellite data because the DNN architectures of data-driven models with more than three layers provide better approximations of nonlinear functions than traditional and shallow neural networks [61]–[64]. Data-driven models can produce more accurate and higher order values if they have more diverse and complex network structures, such as human brain neurons. The advantage of using GOCI imagery for the retrieval of the AOD over land is that it equips shortwave visible channels from blue (>413 nm) to near-infrared (NIR; <670 nm) wavelengths because the spectral surface reflectance is relatively low in the shortwave visible spectral region, decreasing its contribution to TOA reflectance. Therefore, an increase or decrease in the variability due to aerosol reflectance can be detected using GOCI sensors owing to the relatively low intensity of the land surface reflectance in shortwave blue channels.

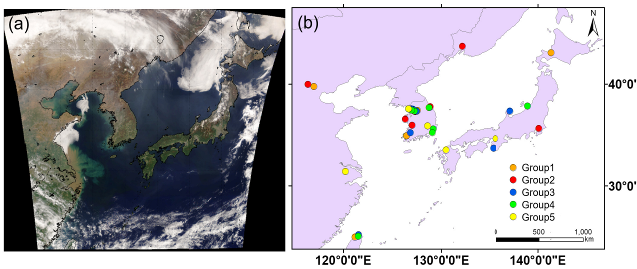

Fig. 1. (a) GOCI RGB composite image acquired on April 20, 2018. (b) Locations of the AERONET sites used as reference data for GOCI AOD retrieval from the data-driven models. Groups separated by color were used for fivefold cross-validation.

II. Data and Study Area

The GOCI sensor onboard the Communication, Ocean, and Meteorological Satellite (COMS) launched in June 2010 is the first geostationary ocean color sensor in the world [65], [66]. COMS is equipped with six visible multispectral bands centered at 412, 443, 490, 555, 660, and 680 nm, and two NIR bands at 745 and 865 nm. Fig. 1(a) shows a full disk RGB image acquired on April 20, 2018, with 2500 km × 2500 km spatial coverage, centered at 36° N, 130° E [66]. This image covers Northeast China, the Korean Peninsula, and Japan, passing over the East Asia domain eight times a day (hourly observations from 00 to 07UTC), with a 500-m spatial resolution. The GOCI satellite, with high spatiotemporal-spectral resolution, is effective for operational air quality monitoring and forecasting because it incorporates data assimilation over Northeast Asia as a near real-time system. The study period was from 2016 to 2018, and the TOA reflectance of GOCI was used as the main input parameter when training the network model, incorporating solar angles, since the upward reflectance at the TOA included not only atmospheric optical properties, including aerosol data, but also land surface data for Lambertian uniform targets [20], [31]. In this study, ground measurements from AERONET stations were used as reference data for the AOD to train and validate the data-driven models. Fig. 1(b) shows the locations of 33 AERONET sites (https://aeronet.gsfc.nasa.gov/) and five groups randomly selected for spatial cross-validation. AERONET is a globally distributed network of Cimel Sun photometers that provide multiwavelength AOD measurements with a low uncertainty of <0.02 [11], [67]. In this study, quality-assured level 2.0 AERONET inversion data [68] were used to evaluate the GOCI AOD values derived from each method. As the Cimel

Sun photometer does not measure radiance at a wavelength of 550 nm, the AOD at 550 nm (τ_{550}) was calculated using a log-linear interpolation with two nearest wavelengths (i.e., 500 and 675 nm) as follows:

$$\tau_{550} = \tau_{500} \times \left(\frac{675}{500}\right)^{-\alpha} \tag{1}$$

where τ_{500} and τ_{675} are the AODs at wavelengths of 500 and 675 nm, respectively; τ_{550} is the AOD at the reference wavelength of 550 nm; and α is the Ångström parameter.

III. METHODS

A. Physical Model-Based AOD Retrieval

The GOCI AOD derived from the physical model-based aerosol retrieval method was compared with that of the DNN model. The physical model-based method uses the dark target approach [14], [15], separation techniques [20], [69], and spectral shape matching [70], [71]. In this method, the aerosol reflectance, $\rho_{\text{aero}}(\lambda, \theta_s, \theta_v, \phi)$, from the GOCI multispectral bands can be determined by subtracting the Rayleigh path reflectance, $\rho_{\text{Ray}}(\lambda, z)$, and surface reflectance, ρ_{Surf}, from the TOA reflectance, $\rho_{\text{TOA}}(\lambda, \theta_s, \theta_v, \phi)$, for given geometrical illumination and observation conditions. The following equation was introduced to determine the aerosol reflectance [20], [31]:

$$\begin{aligned}\rho_{\text{aero}}(\lambda, \theta_s, \theta_v, \phi) &= \rho_{\text{TOA}}(\lambda, \theta_s, \theta_v, \phi) - \rho_{\text{Ray}}(\lambda, z) \\ &\quad - \frac{T_1(\lambda, \mu_s) T_2(\lambda, \mu_v) \cdot \rho_{\text{Surf}}}{1 - \rho_{\text{Surf}} \cdot \rho_{\text{Hem}}(\lambda)}\end{aligned} \tag{2}$$

where $\mu_s = \cos\theta_s$ and $\mu_v = \cos\theta_v$ are the cosine sun zenith angle and cosine viewing zenith angle, respectively; $T_1(\lambda, \mu_s)$ and $T_2(\lambda, \mu_v)$ are the total atmospheric transmittances, including both direct and diffuse transmissions at each of the wavelengths (λ) for the solar and viewing zenith angles, respectively; and $\rho_{\text{Hem}}(\lambda)$ is the hemispheric atmospheric reflectance. In (2), the parameterizations of total transmissions and the hemispheric atmospheric reflectance are given in von Hoyningen-Huene *et al.* [72] and Kokhanovsky *et al.* [73].

To directly determine the theoretical relationship between the multispectral radiances from GOCI and corresponding AOD, the contributions of the Rayleigh path reflectance and surface reflectance can be considered to acquire measurements of the aerosol reflectance from the TOA reflectance in GOCI observations. In (2), the height-dependent Rayleigh path reflectance [$\rho_{\text{Ray}}(\lambda, z)$] can be determined with spectral Rayleigh cross sections and a phase function with respect to the atmospheric pressure, $p(z)$, at elevation z (km) [74]. The estimation of the surface reflectance (ρ_{Surf}) is an ill-posed problem because radiometric interference between atmospheric aerosols and surfaces exists simultaneously. In this study, the GOCI L1b reflectance at 412 nm was used initially to separate the surface reflectance from the TOA reflectance because the surface reflectance at 412 nm is relatively low compared with that of the other GOCI spectral bands, and the influence of the hemispheric reflectance is less effective. As a reference, the initial surface reflectance was estimated based on the 6S radiative transfer model by considering the transmission of the atmospheric gases O_3, NO_2, and H_2O from Ozone Monitoring Instrument (OMI) and National Centers for Environmental Prediction (NCEP) data, without using information of aerosol particles. According to [75], the simplified method based on the 6S radiative transfer model was capable of accurately estimating the spectral surface reflectance, although not incorporating information on aerosol particles and atmospheric gases in terms of real applications.

Although the blue band of GOCI is effective for applying separation techniques, estimating the background surface reflectance with minimal contamination from clouds and aerosols using only a single image remains difficult. Therefore, the minimum surface reflectance with a blue band for a long period was adopted to determine the background surface reflectance under clear sky conditions, assuming that there was at least one clear sky day during the composite period [29], [30], [33], [76]. Furthermore, the minimum surface reflectance was determined when all 10 × 10 pixel blocks were clear pixels to increase the accuracy of finding the clearest homogeneous area. After estimating the initial aerosol reflectance ($\rho_{\text{aero}}^{\text{Sat}}$) of GOCI blue band 1 (412 nm), the spectral AOD of GOCI was theoretically determined by selecting an adequate set of lookup tables (LUTs) describing the relationship between the aerosol reflectance and AOD at 550 nm (τ_{550}). The LUTs were precomputed using clustered aerosol models from selected AERONET sun photometer measurements over the study area using the Santa Barbara discrete ordinance radiative transfer atmospheric radiative transfer (SBDART) model [31], [77]. The AOPs for τ_{550}, spectral aerosol extinction, single scattering albedo, and asymmetry parameters from six aerosol models were used to run the SBDART model to determine the AOD as a function of the aerosol reflectance from GOCI. Finally, spectral shape matching was applied to identify the best matching AOD by comparing it with the precalculated LUTs. To select the optimal aerosol model, the root mean square deviation (RMSD) between the multispectral aerosol reflectance from the GOCI (ρ_{aero}^{m}) and LUTs ($\rho_{\text{aero}}^{c}(\lambda_i)$) at a given sun and sensor geometric condition was estimated as follows:

$$\text{RMSD} = \frac{1}{n} \sum_{i=1}^{n} \left(\frac{\rho_{\text{aero}}^{m}(\lambda_i) - \rho_{\text{aero}}^{c}(\lambda_i)}{\rho_{\text{aero}}^{m}(\lambda_i)} \right) \tag{3}$$

where n is the number of selected wavelengths of GOCI from one to six bands for the AOD over the land surface. The superscripts m and c are the measured and theoretically calculated values, respectively. Spectral shape matching was used at selected bands of 412, 443, 490, 555, 660, and 680 nm to minimize interference by gas absorption and surface reflectance. Until the minimum value of the RMSD satisfied the threshold, the processes mentioned above were repeated to determine the optimal relationship between τ_{550} and ρ_{aero}, and the result was used as the final product of the GOCI AOD (τ_{550}). In this report, we briefly describe the physical model for aerosol retrieval to focus on the assessment of the AOD retrieval using a new deep learning model. Detailed descriptions of the physical model for AOD retrieval, including parameters for the total atmospheric transmittance and hemispheric reflectance, are provided in [31], [71]–[73], and [78].

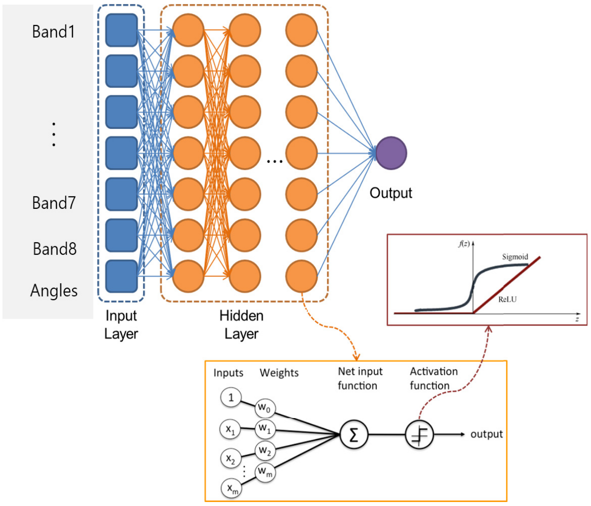

Fig. 2. Schematic of the network structures describing the DNN with a ReLU activation function.

Cloud screening of the GOCI imagery was performed to locate clear sky pixels using a series of threshold tests and a spatial uniformity test [79]. Although inhomogeneous cloud detection degrades the spatial resolution of the final AOD products from 0.5 km × 0.5 km to 5 km × 5 km resolution, it should be applied to improve the accuracy of cloud detection for GOCI satellites without IR channels. Lastly, as the final products for the AOD from the physical model have a resolution of 5 × 5 km after the cloud mask, with a suitable pixel selection of minimum surface reflectance, the same spatial resolution condition was tested in the AOD calculation when using the data-driven models for comparative analysis.

B. Data-Driven Models: DNN, SVR, and RF

The network structure of a DNN consists of one input layer with a number of input parameters, multiple hidden layers with a number of nodes, and an output layer (Fig. 2). The input layer is used as one layer with ten input nodes: the TOA reflectance from eight spectral bands in GOCI and two solar zenith and azimuth angles. For reference, the 500-m spatial resolution of the GOCI spectral bands was aggregated to a 5 × 5 km^2 resolution, which was input into the data-driven models after cloud masking and inhomogeneous tests. The output node of the DNN was 1, which was a reference variable of the AOD (τ_{550}) value from the AERONET measurements. However, the number of hidden layers and nodes changed according to the relationship between the input and output parameters and network structures. In this study, a trial-and-error method was adopted to determine the optimal number of DNN structures [80]. The hidden layer structure under various conditions was tested, and the DNN model with the highest accuracy was determined based on forward and backward propagation. This approach was used because simply complicating or using a deeper network structure does not proportionally increase the retrieval accuracy of the target variable [51]. For the reference, normalization using input and output parameter standardization was adopted to avoid model dependence on different orders of magnitude for each input and output value while training or optimizing the data-driven models. The standard deviations of each input and output were calculated for the training dataset and applied to the validation and test datasets.

In addition, the activation function of each node was used with a rectified linear unit (ReLU) because it is a nonsaturating nonlinearity function with fast convergence of the stochastic gradient descent [81], [82]. To reduce the overfitting of the training data, $L1$ and $L2$ regularization was applied to the DNN model because $L1$ regularization sets some weights close to zero to reduce the complexity, and $L2$ regularization attempts to keep the overall weight close to zero [83]. After the analysis of the DNN network structure, five hidden layers, including 512, 512, 256, 256, and 64 hidden nodes for each layer with $L1$ regularization and batch normalization, showed the highest accuracy for the DNN model and were finally used to estimate the GOCI-based AOD values. Keras, which is a Python deep learning library, was adopted to estimate the GOCI-based AOD, and Bayesian optimization from the Keras Tuner was used to determine the best hyperparameters for the model.

The RF approach is an ensemble algorithm that employs classification and regression trees (CARTs) [84]. The RF model has been used to monitor and predict various atmospheric variables [51], [85]–[87]. The RF generates a multitude of decision trees (1000 trees in this study), and independent trees predict an unknown pixel by aggregating (through averaging or majority voting) the results of the trees [84]. There are two randomization processes in the RF model that are random selections of a subset of the training samples and variables. These processes alleviate the limitations of CARTs, such as the overfitting problem. The *R* software with the RF package (version 0.10.1, default parameter setting) was implemented to develop and apply the RF model.

SVR is a regression version of the support vector machine (SVM) that aims to find an optimal hyperplane to fit the data and predict an unknown pixel. SVR/SVM performs well in modeling small samples and has been widely used in remote sensing [54], [85], [88]–[90]. SVR generally transforms training data from the original feature space into a higher dimension to find an optimum hyperplane [91]. Employing kernel functions, such as linear, polynomial, and Gaussian functions, to separate data effectively is crucial [54]. In this study, SVR was implemented in MATLAB 2018a through the fitrsvm function (https://mathworks.com/help/stats/fitrsvm.html) with the Gaussian kernel function, automatic kernel scaling approach, and "Standardize" module. Although many researchers have used the grid search method to determine the parameters, we employed an automatic kernel scaling approach to select the appropriate parameters based on a heuristic procedure due to the time-consuming nature of the grid search method [92].

C. Performance Metrics of Data-Driven Models

In this study, the performance of each model was evaluated in terms of accuracy, bias, and error using the following selected statistical equations: the root mean square error (RMSE), normalized RMSE, mean bias error (MBE), normalized MBE, index of agreement (IOA), and expected error (EE). The spatial distributions of the AOD retrievals from the four models were compared, and the sensitivity of the error was analyzed. The RMSE, nRMSE, MBE, and nMBE were calculated as follows:

$$\mathrm{RMSE} = \sqrt{\frac{1}{n}\sum_{1}^{n}(\mathrm{AOD}_m - \mathrm{AOD}_o)^2} \tag{4}$$

$$\mathrm{nRMSE} = \mathrm{RMSE}/\sum_{1}^{n}\mathrm{AOD}_o \tag{5}$$

$$\mathrm{MBE} = \frac{1}{n}\sum_{1}^{n}(\mathrm{AOD}_m - \mathrm{AOD}_o) \tag{6}$$

$$\mathrm{nMBE} = \mathrm{nMBE}/\sum_{1}^{n}\mathrm{AOD}_o \text{ and} \tag{7}$$

$$\mathrm{IOA} = 1 - \sum_{1}^{n}(\mathrm{AOD}_m - \mathrm{AOD}_o)^2 \Big/ \sum_{1}^{n}(|\mathrm{AOD}_o - \mathrm{A\bar{O}D}_o| + |\mathrm{AOD}_m - \mathrm{A\bar{O}D}_o|)^2 \tag{8}$$

$$\Delta\mathrm{AOD} = \pm(\text{intercept}) \pm (\text{slope})\mathrm{AOD}_m \tag{9}$$

where AOD_m and AOD_o are the modeled and observed values of AOD at 550 nm, respectively, and $\mathrm{A\bar{O}D}_o$ and $\Delta\mathrm{AOD}$ of EE are the average observed value of the AOD with a sample size of n, and the AOD difference between AOD_m and AOD_o, respectively.

In this study, we evaluated the performances of DNN, SVR, and RF models using two validation approaches: hold-out validation and k-fold cross-validation. For the hold-out validation, we separated the total match-up datasets between the input parameters for the spectral bands and output parameters of the *in situ* AOD into three parts: training data (60%), validation data (20%), and test data (20%), based on the same criteria as the DNN, SVR, and RF models. For the k-fold cross-validation, each data-driven model was validated using the "leave a year out" (threefold cross-validation from 2016 to 2018) and "leave one station out" (fivefold cross-validation for five groups) cross-validation methods to evaluate the temporal and spatial robustness of the models. For the temporal cross-validation, the complete dataset was partitioned into three equal parts for each year (2016, 2017, and 2018). For the spatial cross-validation, 33 stations were randomly grouped into five equal parts (Fig. 1). For both the hold-out validation and the fivefold cross-validation, only the training dataset was used to train each data-driven model, while the validation dataset was used to reduce the overfitting problems associated with data-driven models during training. The remaining test dataset was used to evaluate the performance of each data-driven model for temporal and spatial generalizations of AOD retrieval.

IV. RESULTS AND DISCUSSION

A. Hold-Out Validation of AOD Products From Each Model

Fig. 3 shows the validation results calculated only using the test dataset in a hold-out validation approach. Most match-up points in the SVR, RF, and DNN lie on or near the centered one-to-one reference line, indicating that the data-driven models better matched the AERONET data than the physical model. The AOD results in the data-driven models sufficiently captured the range of the AERONET AOD with a slope of ∼1. The DNN model showed the highest statistical agreement (RMSE = 0.112 and correlation coefficient (R) = 0.863) with the reference AERONET measurements [Fig. 3(c)]. The R, RMSE, MBE, IOA, and EE values were mostly improved in the DNN model. In the physical model, the AOD results showed a good linear relationship, similar to that in the ML models, but the patterns in the scatterplots dispersed for the high AOD value domain. This quantitatively indicated that the slope value (0.16) of the EE from the physical model was higher than those of the ML models.

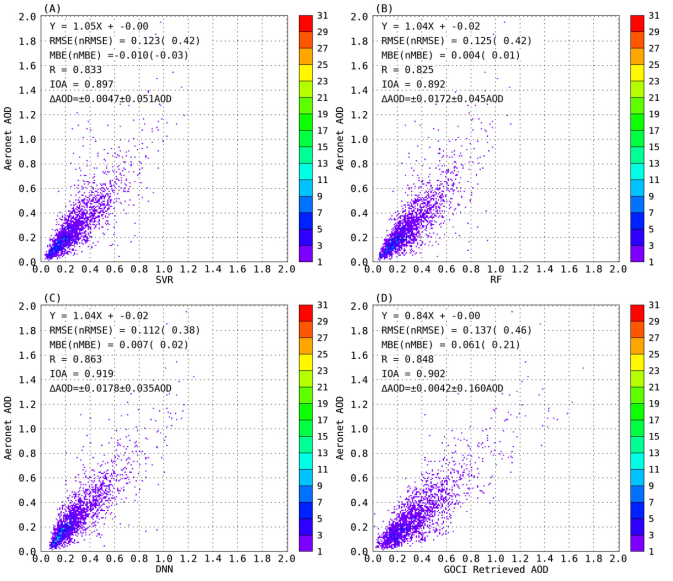

Fig. 3. Density scatterplots of the correlation between the AERONET AOD and satellite imagery-based AOD retrieval models for the (a) SVR, (b) RF, (c) DNN, and (d) physical models.

According to a recent study on GOCI AOD retrieval [30], the statistical values (RMSE = 0.137 and R = 0.848) of the physical model indicated a lower accuracy than those (RMSE = 0.16 and R = 0.91) of GOCI Yonsei aerosol retrieval version 2. The difference between the accuracy of the statistical results in Choi *et al.* [30] and the DNN model in Fig. 3 is significant because traditional physical models still have limitations in separating the reflectance between the aerosols and land surface using the minimum reflectance technique.

B. Temporal and Spatial Cross-Validation of the AOD

The generalization of the suggested models should be evaluated for a reliable estimation of the AOD. Cross-validation has been used to analyze the new data for the AOD that was not included in the training data to identify problems with the data-driven models, such as overfitting [51], [93], as mentioned in Section III.

Table I (temporal cross-validation) and Table II (spatial cross-validation) summarize the statistical results of the cross-validations by year and by station and for each model,

TABLE I

STATISTICAL RESULTS FOR THREEFOLD CROSS-VALIDATION (YEAR)

	SVR	RF	DNN	Physical model
Slope	1.020	1.033	0.970	0.817
R	0.828	0.816	0.833	0.851
RMSE	0.120	0.122	0.118	0.134
nRMSE	0.417	0.423	0.407	0.463
MBE	-0.009	0.004	0.002	–0.061
nMBE	-0.033	0.013	0.007	–0.217
IOA	0.896	0.886	0.904	0.901

TABLE II

STATISTICAL RESULTS FOR FIVEFOLD CROSS-VALIDATION (STATION)

	SVR	RF	DNN	Physical model
Slope	0.986	1.052	0.982	0.804
R	0.752	0.777	0.810	0.842
RMSE	0.143	0.132	0.122	0.134
nRMSE	0.496	0.452	0.416	0.462
MBE	-0.018	0.001	-0.003	0.061
nMBE	-0.064	0.004	-0.010	0.212
IOA	0.834	0.855	0.888	0.891

respectively. The cross-validation results exhibited a lower performance than the hold-out validation results (Fig. 3). The data-driven models showed a higher performance than the physical model, excluding the IOA and R, with an increase of ∼0.2 in the slope and a decrease of 0.012–0.016 (∼0.056) in the RMSE (nRMSE) (Table I). Comparison of the cross-validation results (Tables I and II) between hold-out results (Fig. 3) would mean that that the data-driven models performed poorer than the physical model in terms of the R and IOA owing to the overfitting problem caused by the use of point data as references. The DNN model showed the best performance for most statistical metrics ($R = 0.833$, RMSE = 0.118, MBE = 0.002, and IOA = 0.904) compared with the traditional ML models (Table II). In a previous study producing GOCI-based AOD using RF, the correlation with the AERONET AOD yielded R values of 0.61–0.73, with RMSE values of 0.16–0.27 for the "leave one station out" cross-validation results [38], which are less accurate than the results of this study.

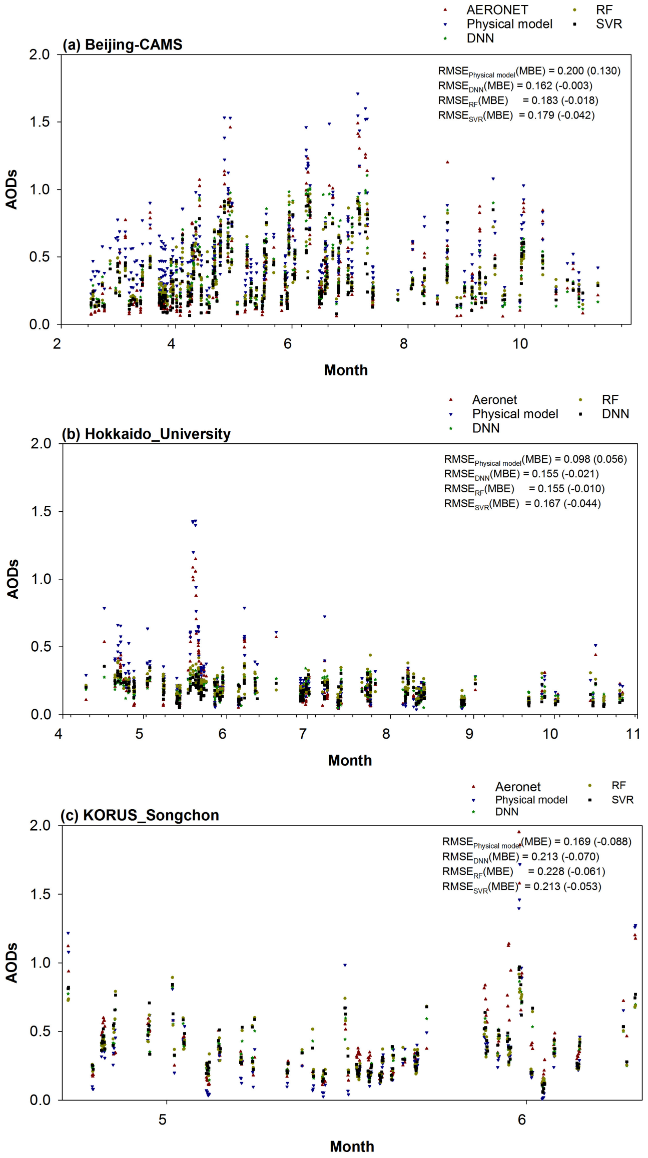

Fig. 4. Comparisons of time series of the AODs from each physical model (dark blue line), DNN (dark green line), RF (dark yellow line), and SVR (black line) with ground-based AERONET measurements (dark red line) for the test dataset in 2016. Three ground stations at (a) Beijing-CAMS, (b) Hokkaido_University, and (c) KORUS_Songchon were selected because they represent the largest standard deviation in the 2016 data at each site. At the Hokkaido_University site, the match-up dataset began from late March due to late snow melting at high latitudes. In case (c), the field campaign period for the Distributed Regional Aerosol Gridded Observation Networks KORUS campaign was from March 31, 2016 to July 1, 2016.

In this study, we also compared the time series of the AODs from each physical model, DNN, RF, and SVR, with ground AERONET measurements to evaluate how well the models captured the abnormal increase or decrease in the AODs for the test dataset in 2016 (Fig. 4). Three ground stations from the Beijing Chinese Academy of Meteorological Sciences (Beijing-CAMS), Hokkaido University, and the KORea-US Air Quality (KORUS) field experiment, Songchon, were selected because they showed the highest standard deviations for the sites in China, Japan, and South Korea in 2016, respectively. The simulated overall temporal variations in the AOPs from the data-driven models matched the AERONET measurements relatively well. However, the physical model overestimated the AOD trends, especially for heavy loads. The DNN was the most accurate model (RMSE (MBE) = 0.162 (−0.003), 0.155 (−0.021), and 0.211 (−0.036) at Beijing-CAMS, Hokkaido University, and KORUS, respectively) among the traditional ML models, but less accurate than the physical model at the Hokkaido University and KORUS sites. Thus, the data-driven models were more accurate than the physical model, but the generalization performance of the ML models remained limited because they used AERONET point data as a reference.

C. Visual Evaluation of AOD Retrievals From Physical and Data-Driven Models

In this study, we compared each data-driven model with the physical model to evaluate their performance visually and to estimate the spatial distribution of the AODs for selected

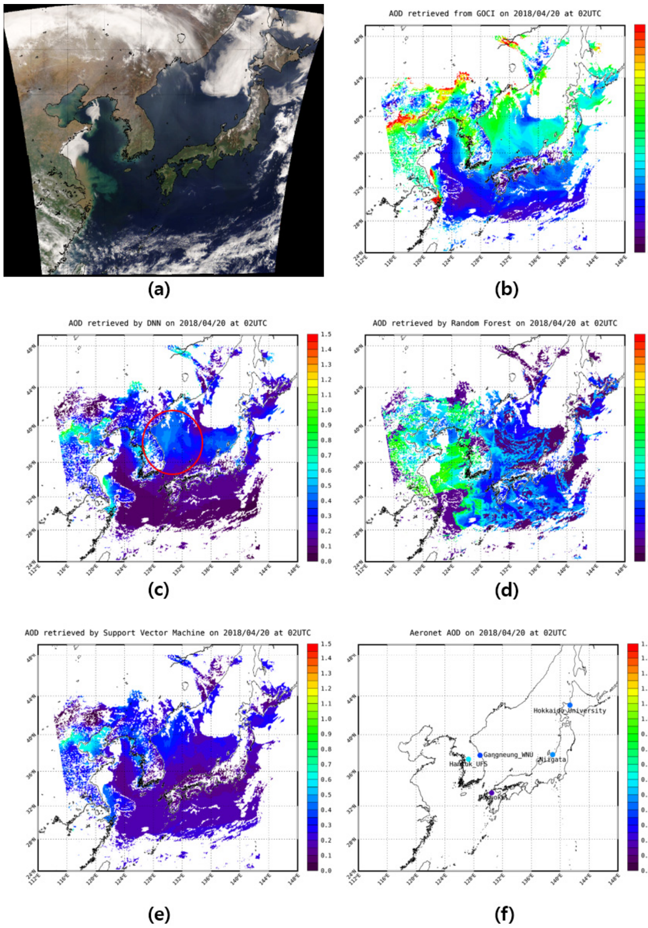

Fig. 5. (a) RGB composite image and estimated AOD maps for the GOCI full disk area from the (b) physical, (c) DNN, (d) RF, (e) SVR models, and (f) corresponding AERONET stations at 02:00 UTC on April 20, 2018. The red circle represents the area with a notable difference in the AOD spatial pattern in the ocean.

cases in the 2018 test dataset. Fig. 5(c)–(f) compares the spatial distributions of the AODs with different intensities obtained using the data-driven models to the corresponding results from the physical model, AERONET stations, and RGB composite image at 02 UTC on April 20, 2018 (Fig. 5). In the DNN model, the spatial pattern of the AOD was well described for clear sky conditions compared with those obtained using the physical model, AERONET stations, and RGB composite image (Fig. 5). The spatial shape of the AOD in the DNN over the ocean in Fig. 5(c) (red circle) matched the results of the physical model and RGB composite image. The RF and SVR results exhibited a spatial pattern similar to that of the DNN results, but with slightly underestimated intensities in the AOD values. When comparing with AOD values from AERONET stations, as shown in Fig. 5(f), the DNN values were more similar to the ground measurements than the RF and SVR values.

In Fig. 6(c)–(f), all of the data-driven models show similar spatial patterns for the AODs, but higher values in the DNN model. Each data-driven model revealed heavy AOPs around thin clouds over land according to visual inspection, despite different intensities in Fig. 6(c)–(e). In the red circle area of Fig. 6(c), they more clearly represent significant differences in the spatial AOD pattern, particularly in heavy AOD regions. Although the physical model showed higher values than the data-driven models [Fig. 6(b)], as well as corresponding statistical results in Fig. 3(d), the spatial patterns of the AOD were more detailed than the RGB composite image from GOCI. This difference existed because the physical model used additional input parameters based on physical theories [70], [71]. In this study, we only used multispectral bands from the GOCI to determine the possibility that the proposed DNN model appropriately simulates the hourly AODs and reveals reliable and competitive statistical results (Fig. 3 and Tables I and II).

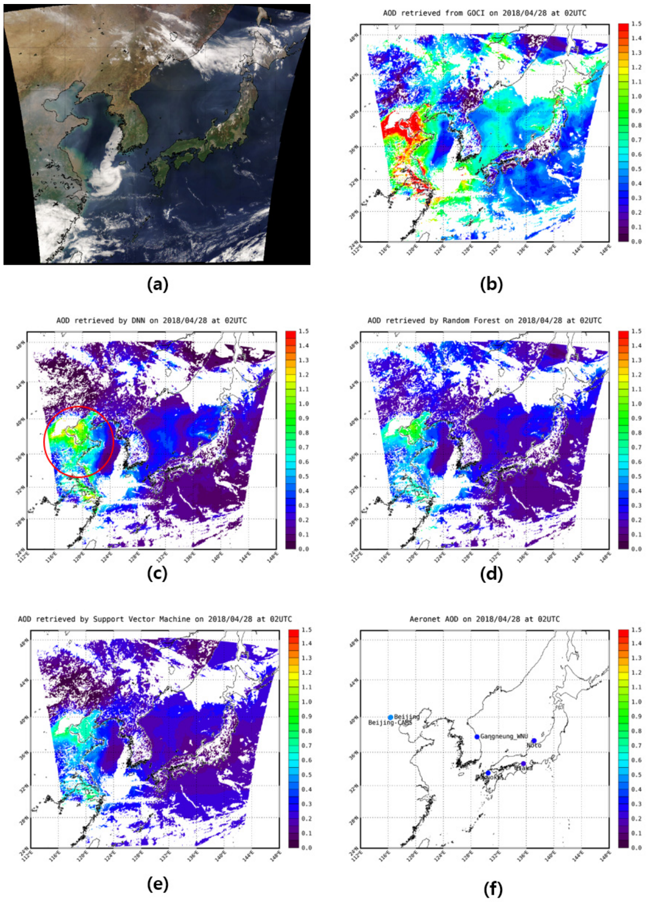

Fig. 6. (a) Composite RGB image and estimated AOD maps for the GOCI full disk area from the (b) physical, (c) DNN, (d) RF, (e) SVR models, and (f) corresponding AERONET stations at 02:00 UTC on April 28, 2018. The red circle represents the area with a significant difference in the AOD spatial pattern over heavy AOD regions over land.

Finally, although the GOCI has the advantage of short visible bands to separate aerosols from the surface due to their low reflectance (blue band at 413 nm), the performance of the cloud mask over the land surface remains a concern because of the absence of the GOCI in the IR channel [Figs. 5(b) and 6(b)]. In future studies, the application of cloud detection algorithms to data-driven models should also be considered for more effective AOD estimation.

V. DISCUSSION

In this study, we evaluated the performance of a DNN model to estimate the AOD by incorporating data from a high temporal resolution geostationary satellite over Northeast Asia from 2016 to 2018. Although the results of the DNN were more consistent with the ground-based AOD data than those of the existing LUT-based physical models, DNNs have some advantages and disadvantages when estimating AOPs using multispectral satellite images from GOCI.

DNNs can simply and directly estimate complicated spatiotemporal AODs using ground measurements and satellite data only, without the need to understand the complicated physical processes of the AOPs. This is an advantage, but also represents the main limitation of DNNs. Unlike the physical model, DNNs do not need ancillary data, such as the background surface reflectance based on the minimum reflectance technique, a climatological database, and AERONET measurements for clustering aerosol models. However, the simple approach of data-driven models may hinder the analysis of AOP radiometric processes based on physical theories because DNNs not only simulate output variables as black boxes [94], but also neglect additional input parameters (i.e., NO_2, O_3, water vapor, air temperature, digital elevation model, additional chlorophyll, wind speed, and direction in the case of the ocean) in their simple approach.

For example, the radiometric characteristics of hygroscopic aerosols can change (e.g., size and chemical components), especially in places where sulfate particles are abundant [95], [96]. This hygroscopic growth effect is neither considered in DNNs nor in ML methods because it is difficult to capture the hysteresis effect of aerosols without training the complicated AOPs processes at the current stage. To sum up, although data-driven models are effective in determining the nonlinear relationship between input and output, physical models should be given priority in case of the inherent AOP analysis.

Another disadvantage of DNNs is that they require large datasets to train network models for generalization performance. Thus, it is difficult to apply DNNs until a sufficient number of training datasets can be obtained, especially during the early operation of a satellite after launch. To overcome this limitation, transfer learning [97] can be used to solve the problems associated with insufficient data samples. Wei *et al.* [98] applied domain-based transfer learning to overcome data scarcity in new, yet related, target domains using knowledge from a domain with a large set of source data. For heterogeneous satellite images, data-based transfer learning was used to solve different dataset specifications at spatiotemporal-spectral resolutions [99]–[101]. However, transfer learning still has limitations compared with existing supervised learning methods, indicating that it can only partially improve the model performance. Therefore, further research is required to solve the data scarcity problem. In addition, a limited number of AERONET stations are one of the disadvantages of data-driven models with respect to the spatial generalization performance, since the AERONET stations [shown in Fig. 1(b)] are few and do not cover various land cover classes or environmental characteristics [102]. Although we performed fivefold cross-validation to evaluate the spatial performance of data-driven models and obtained reliable statistical results, further assessments of data-driven models should be conducted by extending the study area to contain more AERONET stations or by adopting additional input parameters from physical models to enhance the spatial generalization performance of data-driven models in future studies.

TABLE III

COMPUTATION TIME REQUIRED FOR EACH DATA-DRIVEN MODEL TO ESTIMATE A SINGLE IMAGE OF THE AOD USING INPUT PARAMETERS FROM THE GOCI MULTISPECTRAL BANDS

Selected model	AOD calculation time per image	Number of input variables	Computer specifications
Physical model	20 min	20	Intel(R) Core(TM) i7-8809G CPU @ 3.10 GHz
SVR	9 s	10	
RF	1 min 20 s	10	
DNN	8 s	10	

Similar to the limitations of the existing physical models [29], [30], the cloud mask in the GOCI satellite is one of the main problems that must be addressed in the DNN model to acquire reliable environmental monitoring because residual clouds are considered as contaminated data when training network models to estimate the target AOD properties of the land surface. Although GOCI multispectral bands are useful owing to their relatively low surface reflectance contribution, the absence of IR channels in GOCI increases cloud mask errors in the AOP estimation [35]. Thus, input data contaminated by clouds can be used to train or validate the weight vectors of the network models, reducing the accuracy and generalization of the AOD retrieval. Therefore, improvements to the cloud mask should be prioritized to ensure the accuracy of the GOCI AOD in future studies.

The Korea Aerospace Research Institute (KARI) estimates the real-time AOD of the GOCI satellite to calculate the surface reflectance of KOrea Multi-Purpose SATellites 3 and 3A. The main advantage of the DNN model is the shorter calculation time for AOD retrieval in real-time applications. According to Choi *et al.* [30], the physical model is the most limited in near-real-time processing of the AOD because of the high computation load of the spatiotemporal-spectral data from geostationary satellites. The minimum reflectance in (2) is excessively time-consuming when applied to near-real-time systems because the composite of the atmospherically corrected reflectance for each month and hour should be processed over all land areas of Northeast Asia. Table III presents the computation time for each model to estimate a single GOCI image for the AOD. In the physical model, the estimation required 20 min per image, indicating that the model needs a long computation time to process the AOD data retrieved by geostationary satellites. The DNN model had the highest calculation speed for AOD estimation using the input parameters of the GOCI multispectral bands; the computation times for RF, SVR, and DNN were 80, 9, and 8 s, respectively. Although the DNN model required an extended period to optimize the network weights using the match-up dataset, the time necessary to calculate the output parameter was shorter than the training process once learning was completed [35]. However, it needs to be considered that data-driven models are effective in determining the nonlinear relationship between input and output. For reference, the computation time of each data-driven model in Table III was measured using trained and optimized networks for each model. The computation efficiency of each model will vary according to the program code and platform, even for the same model.

Furthermore, the limitations of the generalization performance of data-driven models are demonstrated by the cross-validation results because point data from ground measurements were used as reference values in the models. Nevertheless, there is still room for improvement with respect to data-driven models, i.e., it should be determined how to train them by applying spatial AOD-related variables. A possible solution is that spatial information from the physical model would be considered to enhance the generalization performance of data-driven models. Yuan *et al.* [94] stated that a combined physical–deep learning model not only boosts model accuracy, but also improves the physical understating in environmental remote sensing. Therefore, future research should consider combining DNNs and physical models to estimate target variables effectively according to user purposes.

VI. CONCLUSION

In this study, the AOD over land was estimated using traditional ML models and most advanced DNN method incorporating high temporal-spectral-resolution images from GOCI geostationary satellites. The data-driven models showed more accurate results than the compared models for the AOD, especially for land areas, overcoming the main limitations in aerosol retrieval using the existing LUT-based physical models because physical models cannot effectively separate the reflectance between the atmosphere and the land surface using geostationary satellite data. By incorporating the high-temporal-resolution GOCI satellite data, hourly AOD products were estimated using the data-driven models over Northeast Asia. In both the hold-out validation and cross-validation analyses, the SVR, RF, and DNN showed better performance than the proposed physical model, as well as the methods reported in recent GOCI AOD studies. In the hold-out validation, the DNN model produced the highest RMSE, MBE, and R values of 0.112, 0.007, and 0.873, respectively, compared with the traditional SVR ($\text{RMSE} = 0.123$, $\text{MBE} = -0.010$, and $R = 0.833$) and RF ($\text{RMSE} = 0.125$, $\text{MBE} = 0.004$, and $R = 0.825$). In the cross-validation analysis, although the DNN model showed a lower accuracy than the physical model based on the statistical IOA and R values because of the use of point data as references, it achieved the best performance for most statistical metrics and the highest spatial and temporal generalization performance among the traditional ML models. These findings indicate that deep and complicated neuron structures allow for an accurate simulation of the spatiotemporal distribution of the AOD using limited multispectral GOCI satellite data only. Unlike traditional ML models that have already been fully developed, deep learning has still room for improvement and shows significant potential for applications in environmental science and the interpretation of AOPs.

ACKNOWLEDGMENT

The authors are grateful to the editors and anonymous referees for their helpful comments and suggestions. They also thank the Korea Institute of Ocean Science and Technology (KIOST) for providing the GOCI data.

REFERENCES

[1] R. J. Charlson, J. Langner, H. Rodhe, C. B. Leovy, and S. G. Warren, “Perturbation of the northern hemisphere radiative balance by backscattering from anthropogenic sulfate aerosols,” *Tellus A, Dyn. Meteorol. Oceanogr.*, vol. 43, no. 4, pp. 152–163, Jan. 1991.

[2] T. N. Krishnamurti, B. Jha, J. Prospero, A. Jayaraman, and V. Ramanathan, “Aerosol and pollutant transport and their impact on radiative forcing over the tropical Indian ocean during the January–February 1996 pre-INDOEX cruise,” *Tellus B*, vol. 50, no. 5, pp. 521–542, Nov. 1998.

[3] G. Myhre, F. Stordal, K. Restad, and I. S. A. Isaksen, “Estimation of the direct radiative forcing due to sulfate and soot aerosols,” *Tellus B*, vol. 50, no. 5, pp. 463–477, Nov. 1998.

[4] B. A. Albrecht, “Aerosols, cloud microphysics, and fractional cloudiness,” *Science*, vol. 245, no. 4923, pp. 1227–1230, Sep. 1989.

[5] J. Hansen, M. Sato, A. Lacis, R. Ruedy, I. Tegen, and E. Matthews, “Climate forcings in the industrial era,” *Proc. Nat. Acad. Sci. USA*, vol. 95, no. 22, pp. 12753–12758, 1998.

[6] U. Lohmann and G. Lesins, “Stronger constraints on the anthropogenic indirect aerosol effect,” *Science*, vol. 298, no. 5595, pp. 1012–1015, Nov. 2002.

[7] S. Twomey, “Pollution and the planetary albedo,” *Atmos. Environ.*, vol. 25, no. 12, pp. 2435–3442, Dec. 1974.

[8] C. B. Field, V. R. Barros, K. Mach, and M. Mastrandrea, “Climate change 2014: Impacts, adaptation, and vulnerability,” in *Working Group II Contribution to the IPCC 5th Assessment Report-Technical Summary*. New York, NY, USA: Cambridge Univ. Press, 2014, pp. 1–76.

[9] *Air Quality Guidelines Global Update for Europe*, World Health Organization, Bonn, Germany, 2005.

[10] S. L. K. Unnithan and L. Gnanappazham, “Spatiotemporal mixed effects modeling for the estimation of $PM_{2.5}$ from MODIS AOD over the Indian subcontinent,” *GIScience Remote Sens.*, vol. 57, no. 2, pp. 159–173, Feb. 2020.

[11] B. N. Holben *et al.*, “AERONET—A federated instrument network and data archive for aerosol characterization,” *Remote Sens. Environ.*, vol. 66, no. 1, pp. 1–16, Oct. 1998.

[12] J. Guo *et al.*, “Delaying precipitation and lightning by air pollution over the Pearl River Delta. Part I: Observational analyses,” *J. Geophys. Res. Atmos.*, vol. 121, no. 11, pp. 6472–6488, 2016.

[13] B. Ford and C. L. Heald, “Aerosol loading in the southeastern United States: Reconciling surface and satellite observations,” *Atmos. Chem. Phys.*, vol. 13, no. 18, pp. 9269–9283, Sep. 2013.

[14] Y. J. Kaufman *et al.*, “Operational remote sensing of tropospheric aerosol over the land from EOS-MODIS,” *J. Geophys. Res.*, vol. 102, no. D14, pp. 17051–17068, 1997.

[15] Y. J. Kaufman, A. E. Wald, L. A. Remer, B.-C. Gao, R.-R. Li, and L. Flynn, “The MODIS 2.1-μm channel-correlation with visible reflectance for use in remote sensing of aerosol,” *IEEE Trans. Geosci. Remote Sens.*, vol. 35, no. 5, pp. 1286–1298, May 1997.

[16] R. C. Levy, L. A. Remer, S. Mattoo, E. F. Vermote, and Y. J. Kaufman, “Second-generation operational algorithm: Retrieval of aerosol properties over land from inversion of moderate resolution imaging spectroradiometer spectral reflectance,” *J. Geophys. Res., Atmos.*, vol. 112, no. D13, Jul. 2007, Art. no. D13211.

[17] R. C. Levy *et al.*, “The collection 6 MODIS aerosol products over land and ocean,” *Atmos. Meas. Tech.*, vol. 6, no. 11, pp. 2989–3034, 2013.

[18] L. A. Remer *et al.*, “The MODIS aerosol algorithm, products, and validation,” *J. Atmos. Sci.*, vol. 62, no. 4, pp. 947–973, 2005.

[19] A. M. Sayer *et al.*, “SeaWiFS ocean aerosol retrieval (SOAR): Algorithm, validation, and comparison with other data sets,” *J. Geophys. Res., Atmos.*, vol. 117, no. D3, Feb. 2012, Art. no. D03206.

[20] W. von Hoyningen-Huene, M. Freitag, and J. B. Burrows, “Retrieval of aerosol optical thickness over land surfaces from top-of-atmosphere radiance,” *J. Geophys. Res., Atmos.*, vol. 108, no. D9, May 2003, Art. no. D94260.

[21] W. von Hoyningen-Huene *et al.*, “Retrieval of spectral aerosol optical thickness over land using ocean color sensors MERIS and SeaWiFS,” *Atmos. Meas. Techn.*, vol. 4, no. 2, pp. 151–171, 2011.

[22] L. Mei, V. Rozanov, M. Vountas, J. P. Burrows, R. C. Levy, and W. Lotz, "Retrieval of aerosol optical properties using MERIS observations: Algorithm and some first results," *Remote Sens. Environ.*, vol. 197, pp. 125–140, Aug. 2017.

[23] K. R. Knapp, R. Frouin, S. Kondragunta, and A. Prados, "Toward aerosol optical depth retrievals over land from GOES visible radiances: Determining surface reflectance," *Int. J. Remote Sens.*, vol. 26, pp. 4097–4116, Feb. 2005.

[24] H. Zhang *et al.*, "A multi-angle aerosol optical depth retrieval algorithm for geostationary satellite data over the United States," *Atmos. Chem. Phys.*, vol. 11, no. 23, pp. 11977–11991, 2011.

[25] J. Kim, J.-M. Yoon, M. H. Ahn, B. J. Sohn, and H. S. Lim, "Retrieving aerosol optical depth using visible and mid-IR channels from geostationary satellite MTSAT-1R," *Int. J. Remote Sens.*, vol. 29, pp. 6181–6192, Oct. 2008.

[26] E. Bernard *et al.*, "Description and validation of an AOT product over land at the 0.6 μm channel of the SEVIRI sensor onboard MSG," *Atmos. Meas. Tech.*, vol. 4, no. 11, pp. 254–2565, 2011.

[27] D. Carrer, J.-L. Roujean, O. Hautecoeur, and T. Elias, "Daily estimates of aerosol optical thickness over land surface based on a directional and temporal analysis of SEVIRI MSG visible observations," *J. Geophys. Res.*, vol. 115, no. D10, 2010, Art. no. D10208.

[28] F. Romano, E. Ricciardelli, D. Cimini, F. Di Paola, and M. Viggiano, "Dust detection and optical depth retrieval using MSG SEVIRI data," *Atmosphere*, vol. 4, no. 1, pp. 35–47, Mar. 2013.

[29] M. Choi *et al.*, "GOCI Yonsei aerosol retrieval (YAER) algorithm and validation during the DRAGON-NE Asia 2012 campaign," *Atmos. Meas. Techn.*, vol. 9, no. 3, pp. 1377–1398, Apr. 2016.

[30] M. Choi *et al.*, "GOCI Yonsei aerosol retrieval version 2 products: An improved algorithm and error analysis with uncertainty estimation from 5-year validation over East Asia," *Atmos. Meas. Techn.*, vol. 11, no. 1, pp. 385–408, Jan. 2018.

[31] J. Lee, J. Kim, C. H. Song, J.-H. Ryu, Y.-H. Ahn, and C. K. Song, "Algorithm for retrieval of aerosol optical properties over the ocean from the geostationary ocean color imager," *Remote Sens. Environ.*, vol. 114, no. 5, pp. 1077–1088, May 2010.

[32] Y. M. Govaerts, S. Wagner, A. Lattanzio, and P. Watts, "Joint retrieval of surface reflectance and aerosol optical depth from MSG/SEVIRI observations with an optimal estimation approach: 1. Theory," *J. Geophys. Res.*, vol. 115, no. D2, 2010, Art. no. D02203.

[33] N. C. Hsu, S.-C. Tsay, M. D. King, and J. R. Herman, "Aerosol properties over bright-reflecting source regions," *IEEE Trans. Geosci. Remote Sens.*, vol. 42, no. 3, pp. 557–569, Mar. 2004.

[34] J. V. Martonchik, R. A. Kahn, and D. J. Diner, "Retrieval of aerosol properties over land using MISR observations," in *Satellite Aerosol Remote Sensing Over Land*, A. A. Kokhanovsky and G. de Leeuw, Eds. Chichester, U.K.: Praxis Publishing, 2009, pp. 267–268.

[35] J.-M. Yeom, J.-L. Roujean, K.-S. Han, K.-S. Lee, and H.-W. Kim, "Thin cloud detection over land using background surface reflectance based on the BRDF model applied to geostationary ocean color imager (GOCI) satellite data sets," *Remote Sens. Environ.*, vol. 239, Mar. 2020, Art. no. 111610.

[36] B. L. Lanzaco, L. E. Olcese, G. G. Palancar, and B. M. Toselli, "An improved aerosol optical depth map based on machine-learning and MODIS data: Development and application in South America," *Aerosol Air Qual. Res.*, vol. 17, no. 6, pp. 1623–1636, 2017.

[37] S. Park *et al.*, "Estimation of ground-level particulate matter concentrations through the synergistic use of satellite observations and process-based models over South Korea," *Atmos. Chem. Phys.*, vol. 19, no. 2, pp. 1097–1113, Jan. 2019.

[38] S. Park *et al.*, "Estimation of spatially continuous daytime particulate matter concentrations under all sky conditions through the synergistic use of satellite-based AOD and numerical models," *Sci. Total Environ.*, vol. 713, Apr. 2020, Art. no. 136516.

[39] W. Qin, L. Wang, A. Lin, M. Zhang, and M. Bilal, "Improving the estimation of daily aerosol optical depth and aerosol radiative effect using an optimized artificial neural network," *Remote Sens.*, vol. 10, no. 7, p. 1022, 2018.

[40] M. S. L. Florens, I. H. Cairns, S. A. Knock, and P. A. Robinson, "Data-driven solar wind model and prediction of type II bursts," *Geophys. Res. Lett.*, vol. 34, no. 4, 2007, Art. no. L04104.

[41] M. A. Nielsen, *Neural Networks and Deep Learning*. Canada: Determination Press, 2015.

[42] R. Kumar, R. K. Aggarwal, and J. D. Sharma, "Comparison of regression and artificial neural network models for estimation of global solar radiations," *Renew. Sustain. Energy Rev.*, vol. 52, pp. 1294–1299, Dec. 2015.

[43] K. Mohammadi, S. Shamshirband, M. H. Anisi, K. A. Alam, and D. Petković, "Support vector regression based prediction of global solar radiation on a horizontal surface," *Energy Convers. Manage.*, vol. 91, pp. 433–441, Feb. 2015.

[44] A. Ali, S. E. Amin, H. H. Ramadan, and M. F. Tolba, "Enhancement of OMI aerosol optical depth data assimilation using artificial neural network," *Neural Comput. Appl.*, vol. 23, nos. 7–8, pp. 2267–2279, Dec. 2013.

[45] R. C. Deo, X. Wen, and F. Qi, "A wavelet-coupled support vector machine model for forecasting global incident solar radiation using limited meteorological dataset," *Appl. Energy*, vol. 168, pp. 568–593, Apr. 2016.

[46] R. D. García *et al.*, "Aerosol optical depth retrievals at the Izaña atmospheric observatory from 1941 to 2013 by using artificial neural networks," *Atmos. Meas. Techn.*, vol. 9, no. 1, pp. 53–62, Jan. 2016.

[47] J. Huang, A. Troccoli, and P. Coppin, "An analytical comparison of four approaches to modelling the daily variability of solar irradiance using meteorological records," *Renew. Energy*, vol. 72, pp. 195–202, Dec. 2014.

[48] B. L. Lanzaco, L. E. Olcese, G. G. Palancar, and B. M. Toselli, "A method to improve MODIS AOD values: Application to South America," *Aerosol Air Qual. Res.*, vol. 16, no. 6, pp. 1509–1522, 2016.

[49] T. N. T. Nguyen, S. Mantovani, and P. Campalani, "Validation of support vector regression in deriving aerosol optical thickness maps at 1 km^2 spatial resolution from satellite observations," in *Proc. IEEE Int. Symp. Signal Process. Inf. Technol. (ISSPIT)*, Bilbao, Spain, Dec. 2011, pp. 551–556, doi: 10.1109/ISSPIT.2011.6151623.

[50] G. G. Palancar *et al.*, "Aerosol radiative forcing efficiency in the UV-B region over central Argentina," *Atmos. Res.*, vol. 176, pp. 1–9, 2016.

[51] J.-M. Yeom, S. Park, T. Chae, J.-Y. Kim, and C. S. Lee, "Spatial assessment of solar radiation by machine learning and deep neural network models using data provided by the COMS MI geostationary satellite: A case study in South Korea," *Sensors*, vol. 19, no. 9, p. 2082, May 2019.

[52] G. Mihalakakou, M. Santamouris, and D. N. Asimakopoulos, "The total solar radiation time series simulation in athens, using neural networks," *Theor. Appl. Climatol.*, vol. 66, nos. 3–4, pp. 185–197, Aug. 2000.

[53] P. S. Thenkabail *et al.*, "Selection of hyperspectral narrowbands (HNBs) and composition of hyperspectral twoband vegetation indices (HVIs) for biophysical characterization and discrimination of crop types using field reflectance and hyperion/EO-1 data," *IEEE J. Sel. Topics Appl. Earth Observ. Remote Sens.*, vol. 6, no. 2, pp. 427–438, Feb. 2013.

[54] S. Park, J. Im, S. Park, C. Yoo, H. Han, and J. Rhee, "Classification and mapping of paddy rice by combining landsat and SAR time series data," *Remote Sens.*, vol. 10, no. 3, p. 447, Mar. 2018.

[55] X. X. Zhu *et al.*, "Deep learning in remote sensing: A comprehensive review and list of resources," *IEEE Geosci. Remote Sens. Mag.*, vol. 5, no. 4, pp. 8–36, Dec. 2017.

[56] D. Ciresan, U. Meier, and J. Schmidhuber, "Multi-column deep neural networks for image classification," in *Proc. IEEE Conf. Comput. Vis. Pattern Recognit. (CVPR)*, Washington, DC, USA, Jun. 2012, pp. 3642–3649.

[57] P. Gentine, M. Pritchard, S. Rasp, G. Reinaudi, and G. Yacalis, "Could machine learning break the convection parameterization deadlock?" *Geophys. Res. Lett.*, vol. 45, no. 11, pp. 5742–5751, Jun. 2018.

[58] C. S. Lee, E. Sohn, J. D. Park, and J.-D. Jang, "Estimation of soil moisture using deep learning based on satellite data: A case study of South Korea," *GIScience Remote Sens.*, vol. 56, no. 1, pp. 43–67, Jan. 2019.

[59] S. Scher, "Toward data-driven weather and climate forecasting: Approximating a simple general circulation model with deep learning," *Geophys. Res. Lett.*, vol. 45, no. 22, pp. 12616–12622, 2018.

[60] T. Yang *et al.*, "Evaluation and machine learning improvement of global hydrological model-based flood simulations," *Environ. Res. Lett.*, vol. 14, no. 11, Nov. 2019, Art. no. 114027.

[61] Y. Chen, Z. Lin, X. Zhao, G. Wang, and Y. Gu, "Deep learning-based classification of hyperspectral data," *IEEE J. Sel. Topics Appl. Earth Observ. Remote Sens.*, vol. 7, no. 6, pp. 2094–2107, Jun. 2014.

[62] Y. LeCun, Y. Bengio, and G. Hinton, "Deep learning," *Nature*, vol. 521, no. 7553, p. 436, 2015.

[63] M. Reichstein *et al.*, "Deep learning and process understanding for data-driven Earth system science," *Nature*, vol. 566, pp. 195–204, Feb. 2019.

[64] I. Sutskever and G. E. Hinton, "Deep, narrow sigmoid belief networks are universal approximators," *Neural Comput.*, vol. 20, no. 11, pp. 2629–2636, Nov. 2008.

[65] J.-K. Choi, Y. J. Park, J. H. Ahn, H.-S. Lim, J. Eom, and J.-H. Ryu, "GOCI, the world's first geostationary ocean color observation satellite, for the monitoring of temporal variability in coastal water turbidity," *J. Geophys. Res., Oceans*, vol. 117, no. C9, Sep. 2012, Art. no. C09004.

[66] G. Kang, H. S. Youn, S. B. Choi, and P. Coste, "Radiometric calibration of COMS geostationary ocean color imager," *Proc. SPIE*, vol. 6361, Oct. 2006, Art. no. 636112.

[67] B. N. Holben *et al.*, "An emerging ground-based aerosol climatology: Aerosol optical depth from AERONET," *J. Geophys. Res., Atmos.*, vol. 106, no. D11, pp. 12067–12097, 2001.

[68] O. Dubovik and M. D. King, "A flexible inversion algorithm for retrieval of aerosol optical properties from sun and sky radiance measurements," *J. Geophys. Res., Atmos.*, vol. 105, no. D16, pp. 20673–20696, 2000.

[69] I. L. Katsev, A. S. Prikhach, E. P. Zege, J. O. Grudo, and A. A. Kokhanovsky, "Speeding up the aerosol optical thickness retrieval using analytical solutions of radiative transfer theory," *Atmos. Meas. Techn.*, vol. 3, no. 5, pp. 1403–1422, Oct. 2010.

[70] K. H. Lee, Y. J. Kim, W. von Hoyningen-Huene, and J. P. Burrows, "Spatio-temporal variability of atmospheric aerosol from MODIS data over Northeast Asia in 2004," *Atmos. Environ.*, vol. 41, no. 19, pp. 3959–3973, 2007.

[71] K. H. Lee, M. S. Wong, K. Kim, and S. S. Park, "Analytical approach to estimating aerosol extinction and visibility from satellite observations," *Atmos. Environ.*, vol. 91, pp. 127–136, Jul. 2014.

[72] W. von Hoyningen-Huene *et al.*, "Validation of SCIAMACHY top-of-atmosphere reflectance for aerosol remote sensing using L_1 data," *Atmos. Chem. Phys.*, vol. 7, no. 1, pp. 97–106, Jan. 2007.

[73] A. A. Kokhanovsky, B. Mayer, and V. V. Rozanov, "A parameterization of the diffuse transmittance and reflectance for aerosol remote sensing problems," *Atmos. Res.*, vol. 73, nos. 1–2, pp. 37–43, Jan. 2005.

[74] A. Bucholtz, "Rayleigh-scattering calculations for the terrestrial atmosphere," *Appl. Opt.*, vol. 34, no. 15, pp. 2765–2773, Aug. 1995.

[75] M. Bilal *et al.*, "A simplified and robust surface reflectance estimation method (SREM) for use over diverse land surfaces using multi-sensor data," *Remote Sens.*, vol. 11, no. 11, p. 1344, Jun. 2019.

[76] E. Li, Z. Zhang, Y. Tan, and Q. Wang, "A novel cloud detection algorithm based on simplified radiative transfer model for aerosol retrievals: Preliminary result on Himawari-8 over Eastern China," *IEEE Trans. Geosci. Remote Sens.*, vol. 59, no. 3, pp. 2550–2561, Mar. 2021.

[77] P. Ricchiazzi, S. Yang, C. Gautier, and D. Sowle, "SBDART: A research and teaching software tool for plane-parallel radiative transfer in the Earth's atmosphere," *Bull. Amer. Meteorol. Soc.*, vol. 79, pp. 2101–2114, Oct. 1998.

[78] L. K. Ho, K. Y. Joon, W. von Hoyningen-Huene, and J. P. Burrow, "Influence of land surface effects on MODIS aerosol retrieval using the BAER method over Korea," *Int. J. Remote Sens.*, vol. 27, no. 14, pp. 2813–2830, Jul. 2006.

[79] J. V. Martins *et al.*, "MODIS cloud screening for remote sensing of aerosol over oceans using spatial variability," *Geophys. Res. Lett.*, vol. 29, no. 12, pp. MOD4-1–MOD4-4, 2002.

[80] J.-M. Yeom *et al.*, "Synthetic retrieval of hourly net ecosystem exchange using the neural network model with combined MI and GOCI geostationary sensor datasets and ground-based measurements," *Int. J. Remote Sens.*, vol. 38, no. 23, pp. 7441–7456, Dec. 2017.

[81] A. Krizhevsky, I. Sutskever, and G. E. Hinton, "ImageNet classification with deep convolutional neural networks," in *Proc. Adv. Neural Inf. Process. Syst.*, Lake Tahoe, NV, USA, Dec. 2012, pp. 1097–1105.

[82] V. Nair and G. E. Hinton, "Rectifier linear units improve restricted Boltzmann machines," in *Proc. 27th Int. Conf. Mach. Learn. (ICML)*, Haifa, Israel, Jun. 2010, pp. 807–814.

[83] D. Cook, *Practical Machine Learning with H2O*. Sebastopol, CA, USA: O'Reilly, 2016.

[84] L. Breiman, "Random forests," *Mach. Learn.*, vol. 45, no. 1, pp. 5–32, 2001.

[85] D. Cho, C. Yoo, J. Im, Y. Lee, and J. Lee, "Improvement of spatial interpolation accuracy of daily maximum air temperature in urban areas using a stacking ensemble technique," *GIScience Remote Sens.*, vol. 57, no. 5, pp. 633–649, Jul. 2020.

[86] D. Han, J. Lee, J. Im, S. Sim, S. Lee, and H. Han, "A novel framework of detecting convective initiation combining automated sampling, machine learning, and repeated model tuning from geostationary satellite data," *Remote Sens.*, vol. 11, no. 12, p. 1454, Jun. 2019.

[87] M. Kim, M.-S. Park, J. Im, S. Park, and M.-I. Lee, "Machine learning approaches for detecting tropical cyclone formation using satellite data," *Remote Sens.*, vol. 11, no. 10, p. 1195, May 2019.

[88] Q. Gao and S. Lim, "A probabilistic fusion of a support vector machine and a joint sparsity model for hyperspectral imagery classification," *GISci. Remote Sens.*, vol. 56, no. 8, pp. 1129–1147, 2019.

[89] T. Liu, A. Abd-Elrahman, J. Morton, and V. L. Wilhelm, "Comparing fully convolutional networks, random forest, support vector machine, and patch-based deep convolutional neural networks for object-based wetland mapping using images from small unmanned aircraft system," *GISci. Remote Sens.*, vol. 55, no. 2, pp. 243–264, 2018.

[90] S. Park *et al.*, "Delineation of high resolution climate regions over the Korean peninsula using machine learning approaches," *PLoS ONE*, vol. 14, no. 10, Oct. 2019, Art. no. e0223362.

[91] C. Huang, L. S. Davis, and J. R. G. Townshend, "An assessment of support vector machines for land cover classification," *Int. J. Remote Sens.*, vol. 23, no. 4, pp. 725–749, Nov. 2002.

[92] M. Boardman and T. Trappenberg, "A heuristic for free parameter optimization with support vector machines," in *Proc. IEEE Int. Joint Conf. Neural Netw.*, Vancouver, BC, Canada, Jul. 2006, pp. 610–617.

[93] G. C. Cawley and N. L. Talbot, "On over-fitting in model selection and subsequent selection bias in performance evaluation," *J. Mach. Learn. Res.*, vol. 11, pp. 2079–2107, Jul. 2010.

[94] Q. Yuan *et al.*, "Deep learning in environmental remote sensing: Achievements and challenges," *Remote Sens. Environ.*, vol. 241, May 2020, Art. no. 111716.

[95] G. Feingold, "Aerosol hygroscopic properties as measured by lidar and comparison with *in situ* measurements," *J. Geophys. Res.*, vol. 108, no. D11, p. 4327, 2003.

[96] J. Wang, A. A. Hoffmann, R. J. Park, D. J. Jacob, and S. T. Martin, "Global distribution of solid and aqueous sulfate aerosols: Effect of the hysteresis of particle phase transitions," *J. Geophys. Res.*, vol. 113, no. D11, Art. no. D11206, 2008.

[97] I. Goodfellow, Y. Bengio, and A. Courville, *Deep Learning*. Cambridge, MA, USA: MIT Press, 2016.

[98] Y. Wei, Y. Zheng, and Q. Yang, "Transfer knowledge between cities," in *Proc. 22nd ACM SIGKDD Int. Conf. Knowl. Discovery Data Mining*, San Francisco, CA, USA, Aug. 2016, pp. 1905–1914.

[99] X. Li, L. Zhang, B. Du, L. Zhang, and Q. Shi, "Iterative reweighting heterogeneous transfer learning framework for supervised remote sensing image classification," *IEEE J. Sel. Topics Appl. Earth Observ. Remote Sens.*, vol. 10, no. 5, pp. 2022–2035, May 2017.

[100] B. Huang, B. Zhao, and Y. Song, "Urban land-use mapping using a deep convolutional neural network with high spatial resolution multispectral remote sensing imagery," *Remote Sens. Environ.*, vol. 214, pp. 73–86, Sep. 2018.

[101] X.-Y. Tong *et al.*, "Land-cover classification with high-resolution remote sensing images using transferable deep models," *Remote Sens. Environ.*, vol. 237, Feb. 2020, Art. no. 111322.

[102] M. Shin, Y. Kang, S. Park, J. Im, C. Yoo, and L. J. Quackenbush, "Estimating ground-level particulate matter concentrations using satellite-based data: A review," *GIScience Remote Sens.*, vol. 57, no. 2, pp. 174–189, Feb. 2020.

Jong-Min Yeom received the B.Sc. degree in atmospheric science, the M.S. degree in remote sensing, and the Ph.D. degree from the Department of Environmental Atmospheric Sciences, Pukyong National University, Busan, South Korea, in 2003, 2005, and 2009, respectively. His Ph.D. research focused on exploring the utility of satellite data sensed by sun- and geo-synchronous satellites to retrieve land surface biophysical parameters including nadir BRDF-adjusted reflectance, vegetation indices, and surface insolation.

After his Ph.D. course, he worked as a Post-Doctoral Research Associate beginning in September 2009 under Prof. David Roy at South Dakota State University, Brookings, SD, USA. He is currently with the Korea Aerospace Research Institute, Daejeon, South Korea. His current work is on exploring atmosphere, vegetation, agriculture, land surface, and renewable energy resource incorporating with deep learning and satellite data. He also involves the development of Analysis Ready Data (ARD) products of KOMPSAT-series.

Seungtaek Jeong received the Ph.D. degree from the Department of Applied Plant Science, Chonnam National University, Gwangju, South Korea, in 2018. His Ph.D. research had focused on simulating and monitoring crop information using remote sensing data, including proximity sensors, unmanned aerial vehicle images, and satellite images from the field to continental scales.

He had worked as a Post-Doctoral Researcher at Chonnam National University, and he is currently with the Korea Aerospace Research Institute, Daejeon, South Korea. His current work is to explore the early prediction of crop yield employing a hybrid model that combines a crop model and deep learning using satellite images.

Jong-Sung Ha received the B.S. and M.S. degrees in atmospheric science from Pusan National University, Busan, South Korea, in 2004 and 2006, respectively. His M.S. degree research was aerosol detection using infrared bands of meteorological geostationary satellite.

He is currently with the Korea Aerospace Research Institute, Daejeon, South Korea. He is researching retrieval of atmospheric parameters from geostationary satellites to utilize high-resolution satellite.

Kwon-Ho Lee received the B.Sc. degree from Korea University, Seoul, South Korea, in 1999, and the M.A. and Ph.D. degrees from the Gwangju Institute of Science and Technology, Gwangju, South Korea, in 2001 and 2005, respectively. He has a background in environmental science and engineering, with a specialization in remote sensing.

His research was in satellite remote sensing of atmospheric aerosol studies. In 2005, he was with the Advanced Environmental Monitoring Research Center, Gwangju, for post-doctoral studies in the same field. Since 2006, he has been a Research Associate with the Earth System Science Interdisciplinary Center, University of Maryland, College Park, MD, USA. In 2009, he has also been with the Department of Satellite Geoinformatics Engineering, Kyungil University, Gyeongsan, South Korea. Since 2015, he became a Professor with the Department of Atmospheric Sciences, Gangneung-Wonju National University, Gangneung, South Korea. His areas of interest include atmospheric remote sensing techniques, aerosol optics, radiative transfer models, and radiometric calibration methods. He has authored widely on these topics.

Dr. Lee is a Reviewer for journals specializing in remote sensing and environmental issues.

Chang-Suk Lee received the B.A. and master's degrees in satellite information engineering and the Ph.D. degree in spatial information engineering from Pukyong National University, Busan, South Korea, in 2007, 2009, and 2016, respectively. His Ph.D. research focused on estimating broadband albedo based on COMS/MI geostationary satellite.

He was a Researcher at the National Meteorological Satellite Center to feature analysis and retrieval of soil moisture. He currently works as a Researcher at the Environmental Satellite Center, National Institute of Environmental Research, Ministry of Environment, Incheon, South Korea, since September 2018. He involves in the development and management for GEMS L2 algorithms (total ozone and profile).

Seonyoung Park received the Ph.D. degree from the Ulsan National Institute of Science and Technology (UNIST), Ulsan, South Korea, in 2018.

She worked as a Senior Researcher at the Korea Aerospace Research Institute (KARI), Daejeon, South Korea, from 2018 to 2020. She currently works as a Professor with the Department of Applied Artificial Intelligence, Seoul National University of Science and Technology, Seoul, since September 2020. She have studied remote sensing theories, and applications and state-of-the-art modeling techniques such as artificial intelligence. Her research themes lie in remote sensing-based monitoring and forecasting of extreme weather events, characterization of Earth's surface processes, and water and energy cycles in terms of agriculture and hydrology.